

Real-Time Formulation of Atomistic Electromagnetic Models for Plasmonics

Piero Lafiosca,[†] Luca Nicoli,[†] Silvio Pipolo,[‡] Stefano Corni,^{¶,§} Tommaso
Giovannini,^{*,||} and Chiara Cappelli^{*,†}

[†]*Scuola Normale Superiore, Piazza dei Cavalieri 7, 56126 Pisa, Italy*

[‡]*UCCS Unité de Catalyse et Chimie du Solide, Université de Lille, Université d'Artois UMR 8181,
F-59000, Lille, France*

[¶]*Dipartimento di Scienze Chimiche, Università di Padova, via Marzolo 1, 35131, Padova, Italy*

[§]*Istituto di Nanoscienze del Consiglio Nazionale delle Ricerche CNR-NANO, via Campi 213/A,
41125, Modena, Italy*

^{||}*Department of Physics, University of Rome Tor Vergata, Via della Ricerca Scientifica 1, 00133,
Rome, Italy*

E-mail: tommaso.giovannini@uniroma2.it; chiara.cappelli@sns.it

Abstract

Investigating nanoplasmonics using time-dependent approaches permits shedding light on the dynamic optical properties of plasmonic structures, which are intrinsically connected with their potential applications in photochemistry and photoreactivity. This work proposes a real-time extension of our recently developed fully atomistic approaches ω FQ and ω FQF μ . These methods successfully reproduce quantum size effects in metal nanoparticles, including plasmon shifts for both simple and *d*-metals, even below the quantum size limit. Also, thanks to their atomistic nature and the phenomenological inclusion of quantum tunneling effects, they can effectively describe the optical response of subnanometer junctions. By incorporating real-time dynamics, the approach provides an efficient framework for studying the time-dependent optical behavior of metal nanostructures, including the decoherence of plasmon excitations.

1 Introduction

Under the action of external radiation, the conductive electrons of plasmonic nanomaterials, such as noble metal nanoparticles, can be excited, giving rise to the so-called localized surface plasmons (LSP).¹⁻³ Such plasmons are excited at the plasmon resonance frequency (PRF), which generally shows a high tunability as a function of the size, shape, and chemical composition of the nanostructure.⁴⁻⁷ Such a property, together with the capability of plasmonic materials to absorb a huge amount of energy and the huge enhancement of the electric near field, makes plasmonic materials based on noble metals a unique platform for a plethora of technological applications, ranging from sensing⁷⁻¹⁴ to photocatalysis.¹⁵⁻²⁴

In this context, an in-depth understanding of the dynamics of the optical response of plasmonic structures is vital for elucidating the mechanisms underlying the photophysics and photochemistry of such systems.²⁵⁻²⁷ From the experimental point of view, this can be achieved by resorting to time-resolved spectroscopies.^{28,29} To rationalize the experimental findings, theoretical approaches able to describe the time evolution of the optical response need to be exploited.³⁰⁻³³ The most common theoretical methods generally rely on solving classical Maxwell's Equations or purely quantum mechanical (QM) methods. Classical approaches, such as the Boundary Element Method (BEM)³⁴⁻³⁶ or the Finite-Difference Time-Domain (FDTD) method,^{37,38} are powerful tools for modeling nanoscale optical systems, however, they typically overlook tunneling effects and the atomistic details that are essential for an accurate description of structures defined at the subnanometer levels,³⁹⁻⁴⁸ such as nanojunctions or picocavities.²⁰ On the other hand, QM-based approaches, headed by real-time time-dependent density functional theory (RT-TDDFT) and TDDFT,^{30,49-56} provide a first-principle description of the nanostructure response by retaining the atomistic nature of the system. However, they are computationally prohibitive for large nanosystems and are generally exploited to describe systems composed at most of a few thousand atoms.

To overcome the drawbacks of classical and QM-based approaches, we have recently developed two methods, namely frequency-dependent fluctuating charges (ω FQ)⁵⁷⁻⁶³ and frequency-dependent fluctuating charges and fluctuating dipoles (ω FQF μ).^{64,65} Such methods describe the nanostructure at the full atomistic level and model its optical response by integrating the Drude conduction theory, classical electrodynamics, quantum mechanical tunneling, and interband effects. In particular, in ω FQ, each atom of the nanosystem is

endowed with a charge that dynamically responds to the external field as regulated by the Drude conduction model.^{57,66} In this way, intraband effects are incorporated into the model. To describe *d*-metal nanostructures, we have extended ω FQ by introducing ω FQF μ , where each atom is additionally endowed with a complex polarizability, modeling *d* shell polarizability and interband effects.⁶⁴ In both approaches, we also introduce a phenomenological description of quantum tunneling effects regulating the charge exchange between neighbor atoms.^{44,45} Both ω FQ and ω FQF μ can reproduce reference *ab initio* and experimental data, including plasmon shifts for both simple and noble metals, and atomistically defined nanojunctions, even below the quantum size limit.^{57,64} In other words, they feature accuracy comparable to QM-based approaches, at a much lower computational cost.

In this work, we extend the ω FQ and ω FQF μ models to the real-time (RT) regime, enabling the simulation of the time evolution of plasmonic excitations as driven by light pulses of arbitrary profiles. The resulting RT- ω FQ and RT- ω FQF μ approaches permit the study of the dynamics of the optical response of metal nanostructures, including the decoherence of plasmon excitations. The approaches can describe the response dynamics under short impulses (in the as/fs timescale) and continuous waves (CW) using the same theoretical framework. This is particularly relevant since CW irradiation is often exploited in plasmonic catalysis.^{15,25} We validate the novel approaches by comparing our results with reference *ab initio* TDDFT data for sodium and silver nanostructures. Our method thus offers a comprehensive and efficient tool for studying the dynamics of optical response of metal nanostructures, bridging the gap between classical and QM descriptions, and paving the way for advanced applications in nanophotonics.

The manuscript is organized as follows. In the next section, we report the theoretical derivation of RT- ω FQ and RT- ω FQF μ . The methods are then applied to simulate the time evolution of the optical response of a sodium dimer, displaying a single-atom junction, and a silver icosahedral nanoparticle. The summary and conclusions end the manuscript.

2 Theoretical Model

In this section, we first briefly recall the theoretical foundations of the fully atomistic ω FQ and ω FQF μ approaches for nanoplasmonics. We then present and discuss their extension to the time domain.

2.1 ω FQ and ω FQF μ models

ω FQ is a fully atomistic, classical model that endows each atom of the nanostructure with a frequency-dependent charge.⁵⁷ When an external electric oscillating field is applied to the system, the charge exchange between the atoms is governed by the Drude conduction model. Such an interaction exponentially vanishes by phenomenologically incorporating quantum tunneling mechanisms limiting the charge transfer among the nearest neighboring atoms.⁵⁷ By considering a monochromatic field oscillating at frequency ω , ω FQ charges $q_i(\omega)$ are computed by solving the following equation:⁵⁷

$$\begin{aligned} -i\omega q_i(\omega) &= \frac{2n_0\tau}{1-i\omega\tau} \sum_j^N [1-f(l_{ij})] \frac{\mathcal{A}_{ij}}{l_{ij}} (\phi_j^{el} - \phi_i^{el}) \\ &= \frac{2n_0\tau}{1-i\omega\tau} \sum_j^N K_{ij} (\phi_j^{el} - \phi_i^{el}) \end{aligned} \quad (1)$$

where N is the number of atoms, τ is the friction time, n_0 is the numerical density of the material, \mathcal{A}_{ij} is the effective area connecting i -th and j -th atoms, and l_{ij} is their distance. ϕ_i^{el} is the electrochemical potential on each atom regulating the dynamical polarization of the system. This takes into account the interactions between the atoms and their interaction with the external electric field. Finally, $f(l_{ij})$ is a Fermi-like function mimicking quantum tunneling:⁵⁷

$$f(l_{ij}) = \frac{1}{1 + \exp \left[-d \left(\frac{l_{ij}}{s \cdot l_{ij}^0} - 1 \right) \right]} \quad (2)$$

where l_{ij}^0 is the atom-atom equilibrium distance, whereas d and s determine the sharpness and the center of the damping function, respectively. The parameters entering eq. (1) have a microscopic physical meaning and can be extracted from the experimental permittivity or determined by comparing computed results with reference *ab initio* calculations.^{57,59}

Equation (1) can be recast in a compact way as the following linear system:⁶⁷

$$[\mathbf{A}^{qq} - z_q(\omega)\mathbf{I}_N] \mathbf{q}(\omega) = -\mathbf{f}^q(\omega) \quad (3)$$

where \mathbf{I}_N is the $N \times N$ identity matrix, while \mathbf{A}^{qq} , $z_q(\omega)$ and $\mathbf{f}_q(\omega)$ read:⁶⁷

$$\begin{aligned}\mathbf{A}^{qq} &= (\mathbf{K} - \mathbf{P})\mathbf{T}^{qq} \\ z_q(\omega) &= \frac{1}{2n_0} \left(-\omega^2 - i\omega\frac{1}{\tau} \right) \\ \mathbf{f}^q(\omega) &= (\mathbf{K} - \mathbf{P})\mathbf{V}^{ext}(\omega)\end{aligned}\tag{4}$$

where \mathbf{T}^{qq} is the charge-charge interaction kernel^{57,68} and $\mathbf{V}^{ext}(\omega)$ is the potential associated with the external field evaluated at the position of each atom. The matrix \mathbf{P} takes the following form:⁶⁷

$$P_{ij} = \sum_k K_{ik}\delta_{ij}\tag{5}$$

ω FQ is a fully atomistic approach that models the optical response of nanostructure materials by accounting for intraband mechanisms only, *via* the Drude conduction model. Therefore, the approach cannot describe metals featuring interband transitions, such as noble metal nanostructures.^{69–73} To model these systems, we have recently developed ω FQF μ ,⁶⁴ which extends ω FQ by assigning to each atom of the nanosystem an additional source of polarization, i.e., an atomic polarizability and an associated induced dipole $\boldsymbol{\mu}_i$. The electric potential produced by the dipoles is included in eq. (1) as an external potential acting on the charges in the electrochemical potential ϕ^{el} . The dipoles $\boldsymbol{\mu}_i$ are calculated by solving the following set of linear equations:⁶⁴

$$\boldsymbol{\mu}_i = \alpha^{IB}(\omega) (\mathbf{E}_i^q + \mathbf{E}_i^\mu + \mathbf{E}_i^{ext})\tag{6}$$

where \mathbf{E}^q and \mathbf{E}^μ are the electric fields generated by the charge and the other dipole moments, respectively, while \mathbf{E}^{ext} is the external electric field. $\alpha^{IB}(\omega)$ is the atomic complex polarizability describing interband transitions, which can be easily obtained by extracting interband contributions from the experimental permittivity function.⁶⁴

The equations defining charges and dipoles responses can be coupled together resulting in the following

linear system:⁶⁴

$$\left[\begin{pmatrix} \mathbf{A}^{qq} & \mathbf{A}^{q\mu} \\ \mathbf{T}^{\mu q} & \mathbf{T}^{\mu\mu} \end{pmatrix} - \begin{pmatrix} z_q(\omega)\mathbf{I}_N & \mathbf{0} \\ \mathbf{0} & z_\mu(\omega)\mathbf{I}_{3N} \end{pmatrix} \right] \begin{pmatrix} \mathbf{q}(\omega) \\ \boldsymbol{\mu}(\omega) \end{pmatrix} = \begin{pmatrix} -\mathbf{f}^q(\omega) \\ \mathbf{f}^\mu(\omega) \end{pmatrix} \quad (7)$$

where $\mathbf{T}^{\mu q}$ and $\mathbf{T}^{\mu\mu}$ are the dipole-charge and dipole-dipole interaction kernels,^{64,68,74} while $\mathbf{A}^{q\mu}$, $z_\mu(\omega)$ and $\mathbf{f}^\mu(\omega)$ are defined as:⁶⁴

$$\begin{aligned} \mathbf{A}^{q\mu} &= (\mathbf{K} - \mathbf{P})\mathbf{T}^{q\mu} \\ z_\mu(\omega) &= -\frac{1}{\alpha^{\text{IB}}(\omega)} \\ \mathbf{f}^\mu(\omega) &= \mathbf{E}^{\text{ext}}(\omega) \end{aligned} \quad (8)$$

where $\mathbf{T}^{q\mu} = [\mathbf{T}^{\mu q}]^\dagger$ is the charge-dipole interaction kernel.^{64,68,74}

2.2 Real-Time Extension of ω FQ and ω FQF μ models

In this section, we extend both ω FQ and ω FQF μ to the time domain by proposing their real-time extension.

Let us first focus on ω FQ. Explicating the definition of $z_q(\omega)$ in eq. (3), we obtain:

$$\left(-\frac{\omega^2}{2n_0} - \frac{i\omega}{2n_0\tau} \right) \mathbf{q}(\omega) = \mathbf{A}^{qq}\mathbf{q}(\omega) + \mathbf{f}^q(\omega) \quad (9)$$

By considering the following definition of the Fourier transform

$$\mathcal{F}[f](\omega) = \int_{-\infty}^{\infty} dt e^{i\omega t} f(t), \quad \mathcal{F}^{-1}[f](t) = \frac{1}{2\pi} \int_{-\infty}^{\infty} d\omega e^{-i\omega t} f(\omega) \quad (10)$$

we can rewrite eq. (9) in the time domain by applying \mathcal{F}^{-1} to both sides

$$\frac{1}{2n_0}\ddot{\mathbf{q}}(t) + \frac{1}{2n_0\tau}\dot{\mathbf{q}}(t) = \mathbf{A}^{qq}\mathbf{q}(t) + \mathbf{f}^q(t) \quad (11)$$

where we exploited the following properties of the Fourier transform:

$$\begin{aligned}\dot{\mathbf{q}}(t) &= \frac{1}{2\pi} \int_{-\infty}^{\infty} d\omega e^{-i\omega t} (-i\omega) \mathbf{q}(\omega) \\ \ddot{\mathbf{q}}(t) &= \frac{1}{2\pi} \int_{-\infty}^{\infty} d\omega e^{-i\omega t} (-\omega^2) \mathbf{q}(\omega)\end{aligned}\tag{12}$$

Equation (11) represents the dynamical evolution of a set of coupled forced damped oscillators with the same mass $\frac{1}{2n_0}$ and the same damping parameter $\frac{1}{\tau}$, under the time-dependent force $\mathbf{f}_q(t)$ that depends on the electric potential generated on each charge at the time t . Equation (11) defines the RT- ω FQ approach.

By moving to ω FQF μ , eq. (7) can be rewritten explicating $z_q(\omega)$ and $z_\mu(\omega)$ as follows:

$$\left(-\frac{\omega^2}{2n_0} - \frac{i\omega}{2n_0\tau}\right) \mathbf{q}(\omega) = \mathbf{A}^{qq} \mathbf{q}(\omega) + \mathbf{A}^{q\mu} \boldsymbol{\mu}(\omega) + \mathbf{f}^q(\omega)\tag{13}$$

$$\boldsymbol{\mu}(\omega) = \alpha^{\text{IB}}(\omega) [-\mathbf{T}^{\mu q} \mathbf{q}(\omega) - \mathbf{T}^{\mu\mu} \boldsymbol{\mu}(\omega) + \mathbf{f}^\mu(\omega)]\tag{14}$$

Before applying the inverse Fourier transform, it is convenient to rewrite eq. (14) to avoid the convolution in the time domain in terms of interband polarizability. To this end, we approximate the interband polarizability $\alpha^{\text{IB}}(\omega)$ as a sum of Drude-Lorentz oscillators (DL), similarly to what has been proposed in FDTD^{37,38} and BEM⁷⁵ frameworks:

$$\alpha^{\text{IB}}(\omega) \approx \alpha_{\text{fit}}^{\text{IB}}(\omega) = \sum_p^M \frac{A_p}{\omega_p^2 - \omega^2 - i\omega\gamma_p}\tag{15}$$

where M is the total number of DL oscillators, each of them defined in terms of the parameters A_p , ω_p , and γ_p . We can split eq. (14) by partitioning $\boldsymbol{\mu}(\omega)$ as DL-dependent terms $\boldsymbol{\mu}_p(\omega)$ such that:

$$\boldsymbol{\mu}(\omega) = \sum_p^M \boldsymbol{\mu}_p(\omega)\tag{16}$$

$$\boldsymbol{\mu}_p(\omega) = \frac{A_p}{\omega_p^2 - \omega^2 - i\omega\gamma_p} [-\mathbf{T}^{\mu q} \mathbf{q}(\omega) - \mathbf{T}^{\mu\mu} \boldsymbol{\mu}(\omega) + \mathbf{f}^\mu(\omega)]\tag{17}$$

At this point, the original ω FQF μ problem in eq. (13) and eq. (14) can be recast in $M + 1$ equations in the

frequency domain, i.e.:

$$\begin{aligned} \left(-\frac{\omega^2}{2n_0} - \frac{i\omega}{2n_0\tau}\right) \mathbf{q}(\omega) &= \mathbf{A}^{qq} \mathbf{q}(\omega) + \mathbf{A}^{q\mu} \boldsymbol{\mu}(\omega) + \mathbf{f}^q(\omega) \\ \frac{\omega_p^2 - \omega^2 - i\omega\gamma_p}{A_p} \boldsymbol{\mu}_p(\omega) &= -\mathbf{T}^{\mu q} \mathbf{q}(\omega) - \mathbf{T}^{\mu\mu} \boldsymbol{\mu}(\omega) + \mathbf{f}^\mu(\omega) \end{aligned} \quad (18)$$

By applying \mathcal{F}^{-1} Fourier transform to both charges and dipoles expressions in eq. (18), we finally obtain the $M + 1$ differential equations defining the RT- ω FQF μ model:

$$\frac{1}{2n_0} \ddot{\mathbf{q}}(t) + \frac{1}{2n_0\tau} \dot{\mathbf{q}}(t) = \mathbf{A}^{qq} \mathbf{q}(t) + \mathbf{A}^{q\mu} \boldsymbol{\mu}(t) + \mathbf{f}^q(t) \quad (19)$$

$$\frac{1}{A_p} \ddot{\boldsymbol{\mu}}_p(t) + \frac{\gamma_p}{A_p} \dot{\boldsymbol{\mu}}_p(t) = -\mathbf{T}^{\mu q} \mathbf{q}(t) - \mathbf{T}^{\mu\mu} \boldsymbol{\mu}(t) + \mathbf{f}^\mu(t) - \frac{\omega_p^2}{A_p} \boldsymbol{\mu}_p(t) \quad (20)$$

where we have exploited again the properties recalled in eq. (12).

3 Numerical propagation scheme

To propagate RT- ω FQ and RT- ω FQF μ in time, we exploit a second-order velocity Verlet algorithm in the presence of a friction term.⁷⁶ Note that such a procedure has been previously exploited to deal with similar problems in the context of continuum approaches.⁷⁵ Let us consider a general coordinate system $\mathbf{x}(t)$ described by the following differential equation:

$$\ddot{\mathbf{x}}(t) = \mathbf{F}(t) - \gamma \dot{\mathbf{x}}(t) \quad (21)$$

where \mathbf{F} is the mass-normalized force acting on each coordinate and γ is the friction coefficient. By using a fixed step Δt , the second-order velocity Verlet algorithm scheme expresses $\mathbf{x}(t)$ and the associated velocity $\dot{\mathbf{x}}(t)$ as:

$$\begin{aligned} \mathbf{x}(t + \Delta t) &= \mathbf{x}(t) + \Delta t \left(1 - \gamma \frac{\Delta t}{2}\right) \dot{\mathbf{x}}(t) + \frac{\Delta t^2}{2} \mathbf{F}(t) \\ \dot{\mathbf{x}}(t + \Delta t) &= \left(1 - \gamma \Delta t + \gamma^2 \frac{\Delta t^2}{2}\right) \dot{\mathbf{x}}(t) + \frac{\Delta t}{2} (1 - \gamma \Delta t) \mathbf{F}(t) + \frac{\Delta t}{2} \mathbf{F}(t + \Delta t) \end{aligned} \quad (22)$$

Eq. 22 can be specified for RT- ω FQ and RT- ω FQF μ by defining the mass-normalized time-dependent force acting on charges and dipoles from eqs. (19) and (20):

$$\mathbf{F}^q(t) = 2n_0 [\mathbf{A}^{qq}\mathbf{q}(t) + \mathbf{A}^{q\mu}\boldsymbol{\mu}(t) + \mathbf{f}^q(t)] \quad (23)$$

$$\mathbf{F}_p^\mu(t) = A_p [-\mathbf{T}^{\mu q}\mathbf{q}(t) - \mathbf{T}^{\mu\mu}\boldsymbol{\mu}(t) + \mathbf{f}^\mu(t)] - \omega_p^2\boldsymbol{\mu}_p(t) \quad (24)$$

Note that for RT- ω FQ, only the forces acting on charges are calculated by discarding $\mathbf{A}^{q\mu}\boldsymbol{\mu}(t)$ in eq. (23).

The second-order velocity Verlet algorithm scheme in eq. (22) can finally be specified for the time-propagation of RT- ω FQ as follows:

$$\mathbf{q}(t + \Delta t) = \mathbf{q}(t) + \Delta t \left(1 - \frac{\Delta t}{2\tau}\right) \dot{\mathbf{q}}(t) + \frac{\Delta t^2}{2} \mathbf{F}^q(t) \quad (25)$$

$$\dot{\mathbf{q}}(t + \Delta t) = \left(1 - \frac{\Delta t}{\tau} + \frac{\Delta t^2}{2\tau^2}\right) \dot{\mathbf{q}}(t) + \frac{\Delta t}{2} \left(1 - \frac{\Delta t}{\tau}\right) \mathbf{F}^q(t) + \frac{\Delta t}{2} \mathbf{F}^q(t + \Delta t) \quad (26)$$

In RT- ω FQF μ , the dipoles' time-propagation can be obtained similarly as:

$$\boldsymbol{\mu}_p(t + \Delta t) = \boldsymbol{\mu}_p(t) + \Delta t \left(1 - \gamma_p \frac{\Delta t}{2}\right) \dot{\boldsymbol{\mu}}_p(t) + \frac{\Delta t^2}{2} \mathbf{F}^\mu(t) \quad (27)$$

$$\dot{\boldsymbol{\mu}}_p(t + \Delta t) = \left(1 - \gamma_p \Delta t + \gamma_p^2 \frac{\Delta t^2}{2}\right) \dot{\boldsymbol{\mu}}_p(t) + \frac{\Delta t}{2} (1 - \gamma_p \Delta t) \mathbf{F}^\mu(t) + \frac{\Delta t}{2} \mathbf{F}^\mu(t + \Delta t) \quad (28)$$

4 Computational Details

RT- ω FQ and RT- ω FQF μ equations are solved by using a stand-alone Fortran 95 package. The numerical integration of charges and dipoles is performed by propagating eqs. (25) to (28) from $t = 0$ and by assuming zero initial conditions, which naively correspond to the stationary solution in the absence of external field. ω FQ and ω FQF μ parameters for Na and Ag nanostructures are recovered from Ref. 57 and 64, respectively.

For RT- ω FQF μ , the interband polarizability α^{IB} in eq. (15) is fitted to experimental data by resorting to the Basin-hopping stochastic global optimization algorithm.⁷⁷ The Ag interband polarizability (see Ref. 64 for its definition) is fitted with a different number of DL oscillators ($M = 4, 5, 6, 7$) by minimizing the

residual error:

$$\text{res} = \left| \int_{\omega_{min}}^{\omega_{max}} d\omega \alpha^{\text{IB}}(\omega) - \alpha_{fit}^{\text{IB}}(\omega) \right| \quad (29)$$

where α_{fit}^{IB} is the fitted permittivity that depends on the parameters A_p, ω_p , and γ_p . For each value of M , the optimal parameters are obtained by selecting the best α_{fit}^{IB} from 100 Basin-hopping simulations. Each Basin-hopping simulation is started by setting random values of ω_p extracted in the range between $\omega_{min} = 1$ eV and $\omega_{max} = 7$ eV, A_p and γ_p equal to 1 for each $p = 1, \dots, M$. The fitting procedure is implemented in Python by resorting to the `lmfit` package,⁷⁸ which exploits the Basin-hopping algorithm as implemented in the `scipy` library.⁷⁹ Note that for $M = 6, 7$ the fitting procedure returns some values of $\omega_p \approx 0$ which can potentially generate numerical issues in the time propagation. However, these values can be safely discarded because α_{fit}^{IB} is correctly reproduced in the experimental frequency region of interest (vide infra). Three sets of parameters with $M = 4, 5, 6$ are finally generated. The numerical values of A_p, ω_p , and γ_p are reported in table S1 in the Supporting Information – SI.

5 Numerical Applications

In this section, RT- ω FQ and RT- ω FQF μ approaches are first validated by comparing the absorption spectra as calculated by Fourier-transform the time-dependent responses or by using ω FQ and ω FQF μ defined in the frequency domain. RT- ω FQ and RT- ω FQF μ robustness is further demonstrated by simulating the time-resolved spectral signal of a Sodium dimer characterized by an atomistically defined junction and the dynamical response of an Icosahedral Silver NP and comparing our results with reference *ab initio* data.

5.1 Validation of the propagation scheme

RT- ω FQ and RT- ω FQF μ are validated by computing the optical response of a Sodium cylindrical nanorod (Na_{261} , length 4.968 nm, diameter 1.242 nm, described at the RT- ω FQ level), and a silver spherical NP (Ag_{164} , diameter 1.634 nm, described at the RT- ω FQF μ level). The considered nanostructures are graphically depicted in fig. 1. For both systems, we apply an external electric field described as the following Gaussian-

type kick pulse linearly polarized along the $\hat{\mathbf{x}}$ axis:

$$\mathbf{E}_{\Delta t}^{ext}(t) = E_0 \exp \left[-\frac{(t - t_0)^2}{2(\sigma \Delta t)^2} \right] \hat{\mathbf{x}}, \quad 0 < t < T \quad (30)$$

where $t_0 = 5$ fs, $\sigma = 0.1$, while Δt and T are the time-step and the total evolution time exploited in the time propagation. The Gaussian width depends on Δt in order to have a uniform sampling by varying the time step.

The longitudinal absorption cross-section σ_k along the axis $k = x, y, z$ is computed as:

$$\sigma_k(\omega) = \frac{4\pi\omega}{c} \text{Im}[\alpha_{kk}(\omega)] \quad (31)$$

where ω is the frequency, c is the speed of light and $\alpha_{kk}(\omega)$ is the frequency-dependent polarizability element, which is obtained from the time-propagation dynamics as follows:

$$\begin{aligned} \alpha_{kk}^{\text{RT-}\omega\text{FQ}}(\omega) &= \frac{\int dt \left[\sum_i^N q_i(t) r_{i,k} \right] e^{i\omega t}}{\int dt E_k^{ext}(t) e^{i\omega t}} \\ \alpha_{kk}^{\text{RT-}\omega\text{FQF}\mu}(\omega) &= \frac{\int dt \left[\sum_i^N q_i(t) r_{i,k} + \mu_{i,k}(t) \right] e^{i\omega t}}{\int dt E_k^{ext}(t) e^{i\omega t}} \end{aligned} \quad (32)$$

where q_i is the charge of the i -th atom, whereas $r_{i,k}$, $\mu_{i,k}$ and E_k are the $k = x, y, z$ Cartesian components of the position and the electric dipole of atom i , and the external electric field. The Fourier transform in eq. (32) is numerically computed by resorting to the Fast Fourier Transform as implemented in the `scipy` package.⁷⁹

RT- ω FQ and RT- ω FQF μ longitudinal absorption cross sections of the Na₂₆₁ nanorod and Ag₁₆₄ spherical NP are reported in fig. 1 (top panel), where they are compared to the corresponding $\sigma_x(\omega)$ calculated by exploiting the reference ω FQ and ω FQF μ models, respectively. The relative error on $\sigma_x(\omega)$ obtained from RT- ω FQ(F μ) with respect to ω FQ(F μ) is reported in the bottom panel of fig. 1. In the case of (RT-) ω FQF μ calculations, the fitted interband permittivity α_{fit}^{IB} obtained with $M = 6$ (see table S1 in the SI) is used for both RT- ω FQF μ and ω FQF μ , thus ensuring the same optical response of the system in the two cases.

To validate our integration scheme, the absorption cross-section is calculated by varying the integration

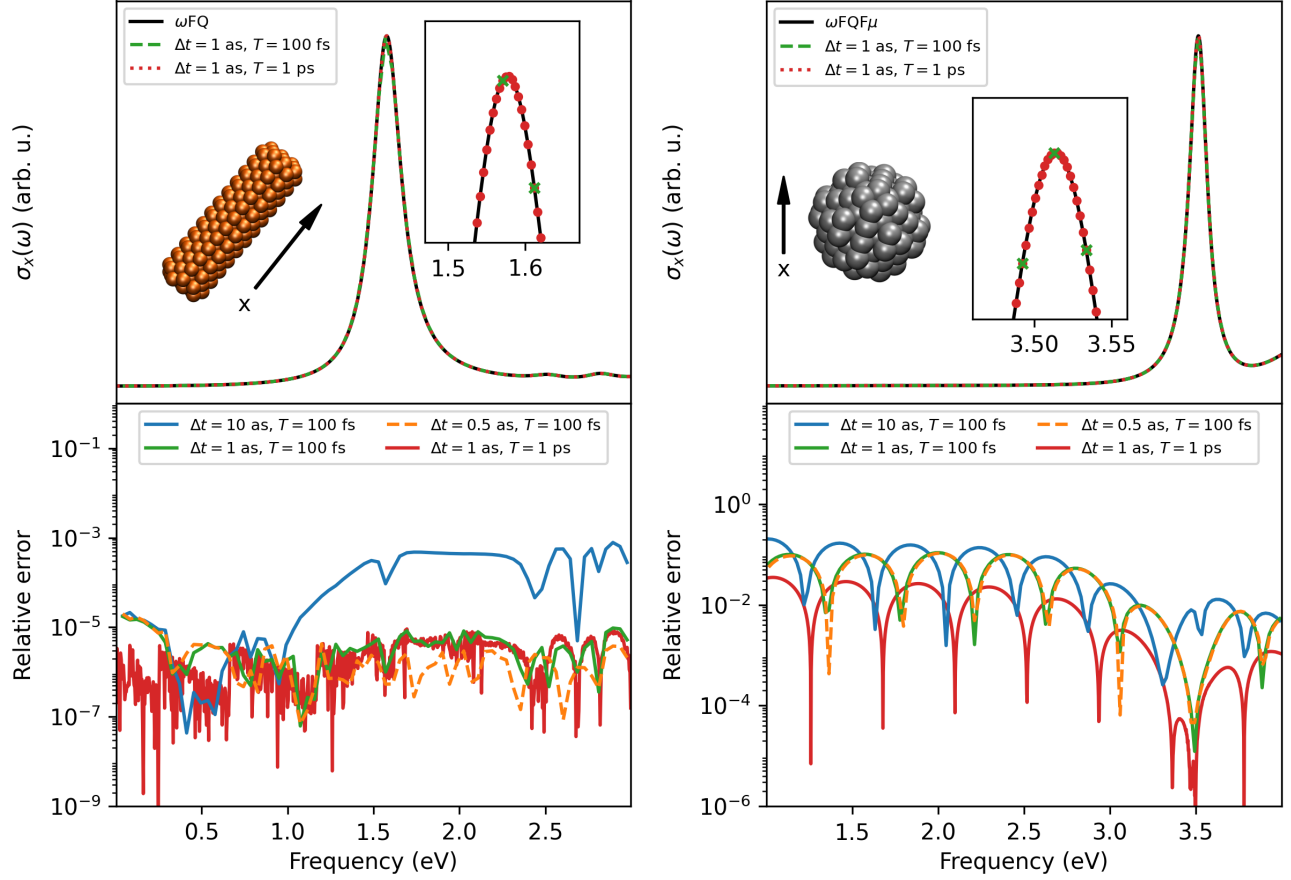


Figure 1: (left) RT- ω FQ and ω FQ absorption cross section (σ_x) of a Na_{261} nanorod as polarized along the x axis. RT- ω FQ results are obtained by varying the parameters of the time evolution (Δt and T) under the action of the external pulse in eq. (30). Relative RT- ω FQ- ω FQ errors are reported in the bottom panel. (right) RT- ω FQF μ and ω FQF μ absorption cross section (σ_x) of a Ag_{164} spherical NP as polarized along the x axis. RT- ω FQF μ results are obtained by varying the parameters of the time evolution (Δt and T) under the action of the external pulse in eq. (30). Relative RT- ω FQ- ω FQ errors are reported in the bottom panel.

time step Δt (0.5, 1, 10 as) and the total simulation time T (100 fs, 1 ps). By first inspecting fig. 1, we note that the numerical results obtained from real-time simulations are qualitatively consistent with the reference values calculated in the frequency domain, perfectly reproducing all the features of the absorption spectrum for both ωFQ and $\omega\text{FQF}\mu$. This is valid for both $T = 100$ fs and $T = 1$ ps, for which the most accurate results are obtained as a higher density of data points is acquired (see inset of fig. 1, top panel).

For a more quantitative analysis, we investigate the relative error obtained for RT- ωFQ and RT- $\omega\text{FQF}\mu$ by taking their frequency-domain counterparts as a reference. Such an analysis is performed for the same input frequencies in both the real-time and frequency-domain calculations. The numerical results are depicted in fig. 1, bottom panel, by varying the numerical parameters of the integration scheme (Δt , T) to quantify their impact on the numerical stability of the simulation. By first focusing on RT- ωFQ (left), we observe that a large Δt (10 as; $T = 100$ fs) is generally associated with the largest errors, in particular in correspondence of the maxima in the absorption spectrum, i.e., for frequencies > 1.5 eV. Differently, all calculations performed by using a smaller time-step (0.5, 1 as; $T = 100$ fs), are associated with a substantial reduction of relative errors for all frequencies and are overall consistent with each other. Interestingly, elongating the total time of the simulation does not significantly affect the numerical errors in the region of the spectrum characterized by absorption peaks.

The relative errors computed for RT- $\omega\text{FQF}\mu$ are inherently higher than those reported for RT- ωFQ by almost 2 orders of magnitude on average. In this case, reducing the time step of the integration does not substantially reduce the relative errors. The most accurate results are obtained by increasing the precision of the Fast Fourier Transform, i.e., by elongating the time simulation of the real-time propagation ($T = 1$ ps), which is associated with an increase in the number of sampled frequencies. This is particularly evident in the significant regions of the spectrum (frequency > 3 eV), where the relative errors are comparable to those reported by RT- ωFQ . The relatively large errors can thus be attributed to limitations in numerical precision.

The discussed analysis validates the accuracy of our implementation and the exploited second-order procedure. In all the following calculations, the time step $\Delta t = 1$ ps is exploited because it guarantees the best compromise between computational cost and accuracy.

5.2 Sodium NP dimer: single-atom junction

As a first test case to analyze the performance of RT- ω FQ, we consider two Na₃₈₀ icosahedral NPs that are connected by a monoatomic junction (see inset in fig. 2). Such structure is extracted from a dynamical simulation of the retraction process of two fused Na₃₈₀ NPs, which has been studied at the full *ab-initio* level by Marchesin et al.⁸⁰ and at the ω FQ level in Ref. 57. The breaking process gradually occurs: the monoatomic junction first arises, and then the dimer dissociates as the distance increases. This study focuses on the monoatomic junction because we have recently shown that tunneling effects are essential to reproduce the *ab initio* reference data.^{57,80} As such, this system represents a perfect test case to show the capabilities of the newly developed RT- ω FQ for studying the dynamics of the optical response of atomistically defined NPs.

In fact, the simulated absorption cross-section along the longitudinal axis of the NP dimer (y) at the ω FQ level is characterized by two main bands.⁵⁷ Such plasmon peaks are associated with two peculiar charge-transfer (CT) plasmonic excitations. The band occurring at 0.34 eV (see A peak in fig. 2) is characterized by a dipolar plasmon in the whole dimer structure. For this reason, it is generally named Charge-Transfer Plasmon (CTP).^{81–83} The second band dominates the spectrum and is especially broad (2 – 4 eV), resulting from the convolution of many absorption peaks. This behavior is commonly identified in most NP dimers.^{41,80,84–86} The associated plasmon shows an overall multipolar character (generally dipolar character by looking at the single nanoparticles), and it is generally called CTP'. The large inhomogeneous broadening reported for the CTP' band is due to transitions with different nodal structure at the atomic scale, but corresponding to plasmons of similar nature (see B, C, D, and E peaks in fig. 2), similarly to what has been reported for other stretched sodium NPs.^{57,84}

To study the plasmon dynamics in the time domain, we resort to RT- ω FQ. We exploit an external cosinusoidal electric field along the dimer axis (y):

$$\mathbf{E}^{ext}(t) = E_0 \cos(\omega_0 t) \hat{y} \quad (33)$$

Differently from section 5.1, the used functional form resembles a continuous wave (CW) illumination of the nanostructure. This demonstrates the flexibility of our approach to describing different excitations,

which can better represent the experimental conditions.^{15,25} The real-time simulation is carried out by using $E_0 = 10^{-6}$ au ($\approx 50\mu\text{V}/\text{\AA}$), $\Delta t = 1$ as, and $T = 50$ fs. In fig. 2, the time propagation of the total dipole moment along the dimer axis μ_y is plotted by setting ω_0 (see eq. (33)) in resonance with A, B, C, D, and E absorption frequencies. The numerical values are normalized with respect to the dipole moments computed at resonance with A absorption, for which the largest μ_y is reported. By looking at fig. 2, we note that the stationary solution is reached for all external frequencies after about 20 fs. In such a time regime, the total dipole moment oscillates in phase with the external field at the forcing frequency, which increases moving from the A to the E band. Remarkably, the relaxation time is similar for each external frequency, since it is intrinsically related to the scattering time assigned to sodium atoms (τ , see eq. (1)). Furthermore, the relative amplitudes of the dipole moments associated with the diverse plasmon excitations are directly connected with the imaginary part of the polarizability of the system, which in turn is related to the absorption cross section reported in fig. 2 through eq. (31). This is why the largest amplitudes are reported for ω_0 in resonance with the A peak, and the relative amplitudes decrease by increasing the external frequency, following the trends highlighted by the absorption spectrum.

Our real-time model also allows for graphically investigating the dynamical oscillation of the plasmonic excitation. A similar study has also been performed at the *ab initio* level as derived from TDDFT calculations, assuming a periodic oscillation equal to $2\pi/\omega_0$.⁸⁰ RT- ω FQ gives direct access to this analysis, allowing an in-depth investigation of the dynamics of the plasmon. In this case, we focus on plasmonic dynamics once the system enters the stationary condition. Such a time evolution is depicted in fig. 3 for the CTP peak at 0.34 eV (all the other time evolution are graphically depicted in figs. S2 to S5 in the SI). As can be noticed, the single-atom junction behaves as an accumulation point for electron conduction, limiting the charge transfer between the two structures. Such a structure is associated with a substantial reduction of the electron current across the single-atom junction at both the ω FQ and TDDFT levels.^{57,80} We finally remark that the plasmon dynamics in fig. 3 qualitatively reproduces the TDDFT behavior⁸⁰ at a much lower computational cost.

5.3 Icosahedral Ag NP

Let us now consider the intricate case of *d*-metal nanostructures, for which a proper description of interband transitions is crucial to reproduce the correct experimental optical properties.⁶⁴ As explained in section 2.2,

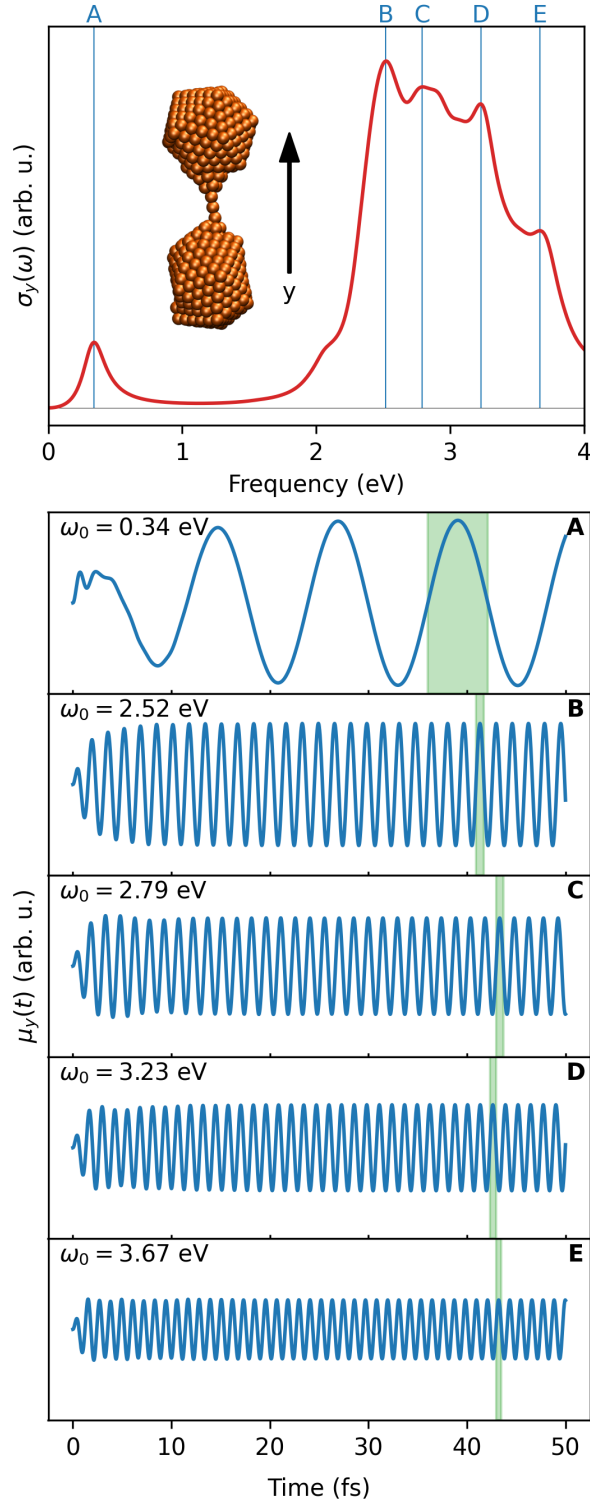


Figure 2: (top) ω FQ absorption cross section of Na₃₈₀ dimer as polarized along the y axis. (bottom) RT- ω FQ total dipole moment induced in the y direction as a function of time for A, B, C, D, and E peaks highlighted in the top panel.

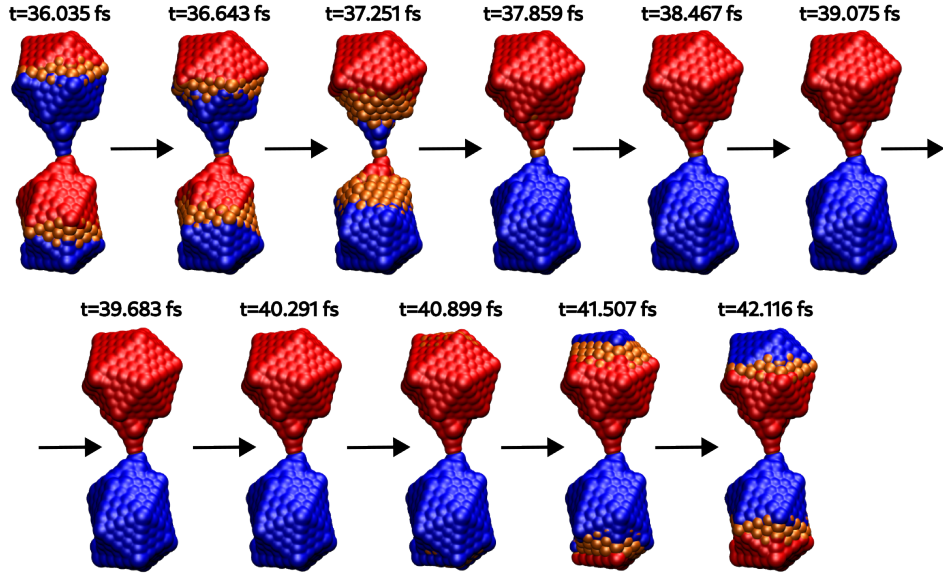


Figure 3: RT- ω FQ time evolution of the plasmon excitation of Na₃₈₀ dimer excited using a monochromatic field oscillating at 0.34 eV (A peak in fig. 2, top panel). The plasmon oscillation is reported for the time region highlighted in green in fig. 2, bottom panel. The isovalue is set to 0.001 au.

in order to study the dynamics of ω FQF μ plasmonic response, we approximate the interband polarizability $\alpha^{IB}(\omega)$ as a sum of M DL oscillators. The number M of DL oscillators is chosen to ensure the accurate reproduction of the interband polarizability. To select the minimum number of DL required for this purpose, in fig. 4 (left) we report α_{fit}^{IB} as fitted by exploiting 4, 5, and 6 DL oscillators. For all cases, the reproduction of the experimental polarizability is particularly satisfactory, especially for frequencies larger than 4 eV. Some larger discrepancies are instead observed for smaller frequencies (1-4 eV), because $\alpha^{IB}(\omega)$ imaginary part is close to zero, and the DL functional form is not ideal in this case. The numerical fitting values are reported in table S1 in SI. Note however that in such a region the optical response is dominated by intraband transitions, thus the effect of interband transitions is expected to be small. It is also worth pointing out that some amplitudes A_p are negative (as also obtained in ref. 75), however, the overall sign of the interband polarizability is positive.

To further evaluate the accuracy of the fitting procedure, in fig. 4 (right), the absorption cross-section of an Ih Ag NP constituted of 561 atoms (Ag₅₆₁, radius ~ 1.4 nm) is computed at the RT- ω FQF μ level ($\Delta t = 1$ as, $T = 500$ fs) by exploiting $\alpha^{IB}(\omega)$ fitted using $M = 4, 5, 6$ DL oscillators. ω FQF μ spectrum calculated in the frequency domain by using the experimental interband polarizability is taken as a reference (black line in fig. 4, right). The results clearly show that an accurate reproduction of the ω FQF μ spectrum is achieved

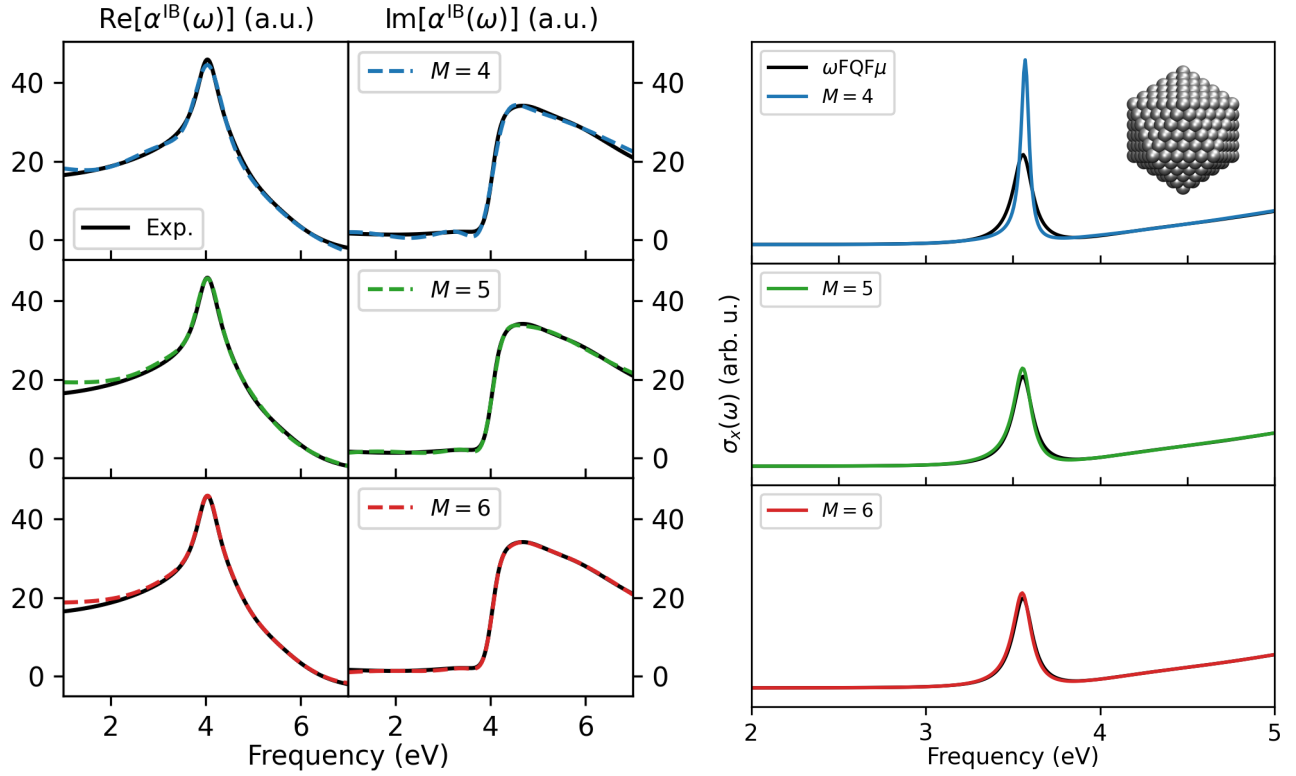


Figure 4: (left) Fitting of the experimental interband polarizability $\alpha^{\text{IB}}(\omega)$ by using $M = 4, 5, 6$ DL oscillators (see eq. (15)). (right) RT- $\omega\text{FQF}\mu$ absorption cross section using α^{IB} as fitted using $M = 4, 5, 6$ DL oscillators. $\omega\text{FQF}\mu$ reference spectrum as calculated by using the experimental α^{IB} is also reported for comparison's sake.

when $M > 4$ DL oscillators are exploited in the fitting procedure. In fact, $M = 4$ (top panel) provides an overall good description of the $\omega\text{FQF}\mu$ spectrum, however, the maximum intensity of the plasmon peak (at about 3.5 eV) and its width are wrongly predicted (the intensity is almost twice the reference, the width is smaller). Indeed, our results remark on the crucial importance of a proper modeling of the interband transitions to reproduce the optical properties of noble metal NPs, highlighting how small differences in the interband polarizability can drastically affect the optical response. As a final comment, it is worth pointing out that the outlined discrepancies are associated with the diverse description of the interband polarizability. This is demonstrated by the perfect agreement between $\omega\text{FQF}\mu$ and RT- $\omega\text{FQF}\mu$ spectra computed by using the same permittivity function (see fig. S1 in the SI).

To further demonstrate the reliability and robustness of our newly developed RT- $\omega\text{FQF}\mu$ approach, we simulate the time evolution of the plasmonic excitation of Ag_{561} 1h NP under the effect of the following ultrafast Gaussian light pulse:

$$\mathbf{E}^{ext}(t) = E_0 \cos(\omega_0(t - t_0))e^{-(t-t_0)^2/(2\sigma^2)}\hat{\mathbf{x}} \quad (34)$$

where $E_0 = 51 \mu\text{V}/\text{\AA}$ and $\sigma = 2.121$ fs. ω_0 is set to the PRF (3.5 eV). The parameters are chosen to match the *ab initio* RT-TDDFT study performed by Rossi et al.³⁰ on the same structure. Their *ab initio* results are thus taken as a reference for challenging RT- $\omega\text{FQF}\mu$. A graphical depiction of the exploited impulse is given in fig. 5, where the computed RT- $\omega\text{FQF}\mu$ dipole as a function of time is also reported. The light pulse triggers a plasmonic response by generating a pronounced dipole moment within the system, which arises after a few femtoseconds (see fig. 5a). As the system evolves in time, specifically when t approaches 13 fs, the system undergoes a dephasing process. The coherence of the plasmon oscillations deteriorates, leading to a gradual decay of the dipole moment. The picture outlined by RT- $\omega\text{FQF}\mu$ perfectly matches the reference *ab initio* RT-TDDFT time evolution (see fig. 5b). The agreement between the classical and quantum methods is excellent, not only qualitatively, but also quantitatively. In fact, only minor discrepancies are observed. The time delay of the plasmonic response for RT- $\omega\text{FQF}\mu$ is smaller than RT-TDDFT as highlighted by vertical 1-3 bars in fig. 5a-b. In addition, RT- $\omega\text{FQF}\mu$ predicts a larger induced dipole moment, but of the same order of magnitude (~ 0.035 e \AA vs. ~ 0.022 e \AA). This result is particularly remarkable, especially considering

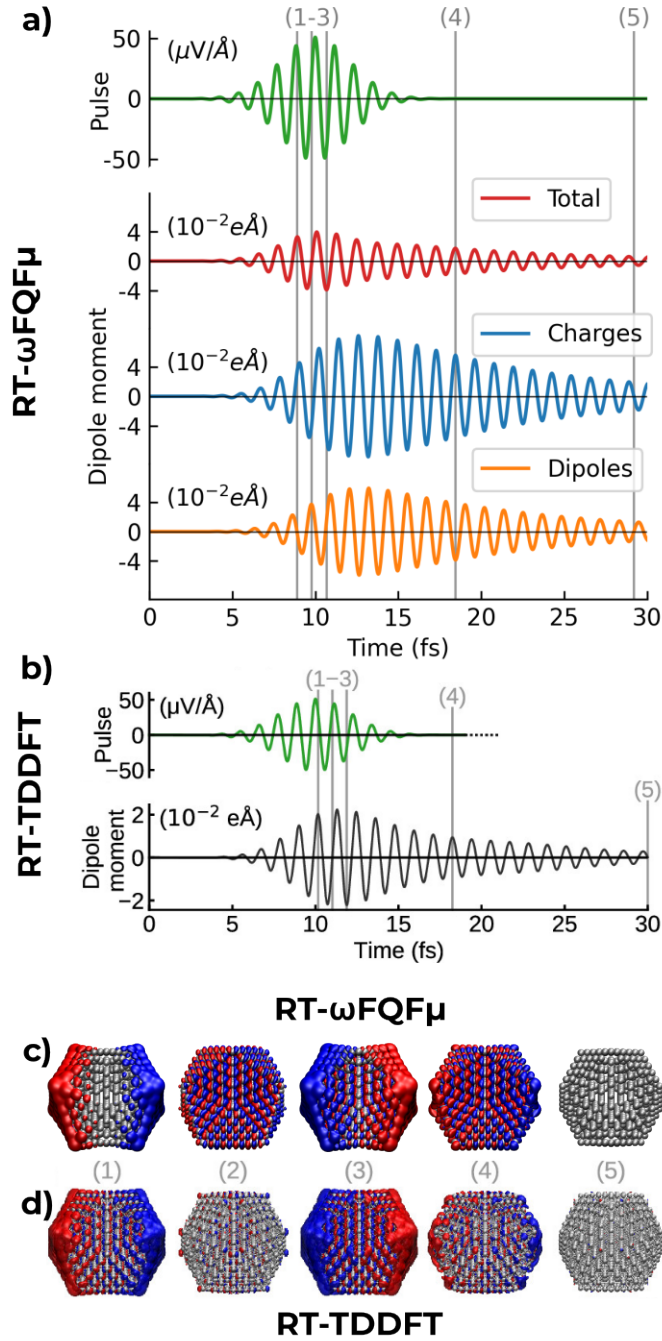


Figure 5: (a-b) RT- ω FQF μ (a) and RT-TDDFT³⁰ (b) time evolution of the plasmon excitation of Ag_{561} Ih NP excited using a monochromatic Gaussian pulse (top panel). In panel a, the total RT- ω FQF μ response (red) is also decomposed in charge (blue) and dipole (orange) components. (c-d) RT- ω FQF μ (c) and RT-TDDFT³⁰ (d) plasmon densities at specific times (1-5) as depicted in panels a-b, respectively. The iso-value is set to 0.035. RT-TDDFT data in panels b and d are adapted with permission from Ref. 30.

the classical nature of RT- ω FQF μ and the associated low computational cost.

To quantify the effective decay timing τ associated with the dephasing mechanisms, we fit the RT- ω FQF μ and RT-TDDFT curves by using $e^{-t/\tau}$ functional form. The resulting RT- ω FQF μ τ is 9.6 fs, showing a typical localized surface plasmon decay time. This is in very good agreement with the reference *ab initio* fitted τ value (7.8 fs). Therefore, RT- ω FQF μ can be as accurate as RT-TDDFT in describing the plasmonic time evolution and decay, even for nanostructures below the quantum size limit, where it is commonly accepted that an explicit quantum description is necessary. The small numerical discrepancy can be due to the fact that RT- ω FQF μ does not account for electron-surface scattering damping mechanisms^{64,87,88} thus modifying the final numerical value of τ .

The fitted τ substantially differs from the Drude scattering time exploited to model intraband mechanisms in our RT- ω FQF μ calculations (~ 39 fs). Such a finding suggests that interband effects play a non-trivial role in determining the time evolution of the response of the plasmonic decay. This is expected since interband transitions determine the optical response of noble nanostructures as demonstrated in fig. 4. In fact, the interband relaxation in Ag nanostructures is governed by the inverse of γ_p in eq. (20) (see also table S1 in the SI). For $M = 6$ DL oscillators, the scattering times ($1/\gamma_p$) range from 4.5 as to 30.5 as. Therefore, intra and interband decay mechanisms non-trivially interplay, resulting in the fitted τ value. To deepen on this point, in fig. 5a, the RT- ω FQF μ time evolution of the total dipole moment is decomposed in its charge and dipole contributions. In fact, our classical approach allows for dissecting the contributions from delocalized and d electrons. This is possible thanks to the formulation of RT- ω FQF μ in terms of charges and dipoles with a clear physical meaning being directly associated with intra and interband mechanisms, respectively.⁶⁴ Figure 5a shows that charges and dipole dynamics are inherently connected, generally oscillating in counter phase for the whole duration of the plasmonic excitation (especially for $t > 13$ fs). Also, note that both charge and dipole decay with the same effective time, although the time scattering related to the two underlying mechanisms is defined in two different timescales. This is not surprising considering that charges and dipoles act as coupled oscillators in our model (see eqs. (19) and (20)). However, their dynamics non-trivially couple, thus resulting in the total dipole moment time evolution which has been previously discussed.

To further investigate this point, we analyze the time evolution of the plasmonic response by plotting the plasmon densities at relevant times (see 1-5, in fig. 5a,b), which are given in fig. 5c. The RT-TDDFT

plasmon densities, reproduced from Ref. 30, are given in fig. 5d as a reference. The plasmonic excitation is characterized by electron density oscillations, which can be dissected into two main components. The first component is a surface-to-surface element, predominantly associated with delocalized valence electrons and intraband mechanisms. These electrons exhibit collective behavior and mainly determine the overall electron density oscillations. The second component arises from atom-localized contributions, which are linked to the screening effect due to interband transitions originating from the d -band. The plasmon decay (plots 4-5 in fig. 5c) is directly correlated with the diminishing surface-to-surface electron density oscillations, marking the end of the collective plasmonic activity. The intricate interplay between the delocalized valence electrons and the localized d -band electrons therefore forms the basis of the observed electron density oscillations. By comparing RT- ω FQF μ and RT-TDDFT, we note that such an interplay is correctly reproduced by our classical RT- ω FQF μ approach, thanks to the proper inclusion of intraband and interband decay mechanisms.

6 Summary and Conclusions

In this work we have presented two novel approaches, namely RT- ω FQ and RT- ω FQF μ , to describe the time evolution of plasmonic excitations in simple and noble metal nanoparticles. The developed methods are the real-time extension of ω FQ and ω FQF μ , which have been previously developed in the frequency domain. Such models provide an accurate fully atomistic modeling of plasmonic nanoparticles, by properly describing intra and interband effects and also tunneling mechanisms. Our real-time extension can handle short impulses (in the as/fs timescale) and CW within the same theoretical formulation.

RT- ω FQ and RT- ω FQF μ are first numerically validated taking the frequency-domain counterparts' results as reference. Then the models have been tested against two different challenging nanostructures: a sodium dimer characterized by a single atom junction, and an Ih Ag NP. To show the flexibility of our implementation, the first system is studied under CW illumination, while a Gaussian pulse is used to excite the Ag NP. As a result, while in the first case, after a transient, the total dipole moment of the nanostructure oscillates in phase with the external CW field, Ag NP total dipole moment is first excited and then fast decays in the fs timescale. In the latter, we directly compared with *ab initio* RT-TDDFT, demonstrating a qualitative and even quantitative agreement between our classical and the quantum approach. As a consequence, our approach

can serve as a powerful approach for simulating the plasmonic response dynamics even for NP size below the quantum size limit. We note that we can further increase the agreement between our approach and full quantum treatments by including electron surface scattering damping decay mechanisms, which can serve as an additional decay channel.⁸⁷

The development of RT- ω FQ and RT- ω FQF μ paves the way for the investigation of the decoherence of the plasmonic response in nanostructures of sizes considerably larger than those that can be treated at the purely quantum level, without losing accuracy. Also, the model has the potential to be coupled to a QM description of molecular systems adsorbed on metal nanostructures,⁶³ as previously done in the frequency domain^{89,90} or by using diverse electrodynamic approaches.^{75,91–94} Such an extension will be the topic of future papers.

Acknowledgments

We thank Giulia Dall’Osto for the discussions on the dielectric function fitting. We gratefully acknowledge the Center for High-Performance Computing (CHPC) at SNS for providing the computational infrastructure.

Funding Sources

This work has received funding from the European Research Council (ERC) under the European Union’s Horizon 2020 research and innovation programme (grant agreement No. 818064). SC thanks the Horizon 2020 EU grant ProID (grant agreement No. 964363) for funding.

Supporting Information Available

Numerical values of A_p , ω_p , and γ_p for $M = 4, 5, 6$ DLs. Graphical depiction of plasmon time evolution for B, C, D, and E peaks depicted in fig. 3.

References

- (1) Pitarke, J.; Silkin, V.; Chulkov, E.; Echenique, P. Theory of surface plasmons and surface-plasmon polaritons. *Rep. Prog. Phys.* **2006**, *70*, 1.
- (2) Giannini, V.; Fernández-Domínguez, A. I.; Heck, S. C.; Maier, S. A. Plasmonic nanoantennas: fundamentals and their use in controlling the radiative properties of nanoemitters. *Chem. Rev.* **2011**, *111*, 3888–3912.
- (3) Halas, N. J.; Lal, S.; Chang, W.-S.; Link, S.; Nordlander, P. Plasmons in strongly coupled metallic nanostructures. *Chem. Rev.* **2011**, *111*, 3913–3961.
- (4) Kelly, K. L.; Coronado, E.; Zhao, L. L.; Schatz, G. C. The optical properties of metal nanoparticles: the influence of size, shape, and dielectric environment. *J. Phys. Chem. B* **2003**, *107*, 668–677.
- (5) Liz-Marzán, L. M. Tailoring surface plasmons through the morphology and assembly of metal nanoparticles. *Langmuir* **2006**, *22*, 32–41.
- (6) Ringe, E.; McMahon, J. M.; Sohn, K.; Cogley, C.; Xia, Y.; Huang, J.; Schatz, G. C.; Marks, L. D.; Van Duyne, R. P. Unraveling the effects of size, composition, and substrate on the localized surface plasmon resonance frequencies of gold and silver nanocubes: a systematic single-particle approach. *J. Phys. Chem. C* **2010**, *114*, 12511–12516.
- (7) Langer, J. et al. Present and Future of Surface-Enhanced Raman Scattering. *ACS Nano* **2020**, *14*, 28–117.
- (8) Willets, K. A.; Van Duyne, R. P. Localized surface plasmon resonance spectroscopy and sensing. *Annu. Rev. Phys. Chem.* **2007**, *58*, 267–297.
- (9) Zhang, R.; Zhang, Y.; Dong, Z.; Jiang, S.; Zhang, C.; Chen, L.; Zhang, L.; Liao, Y.; Aizpurua, J.; Luo, Y.; Yang, J. L.; Hou, J. G. Chemical mapping of a single molecule by plasmon-enhanced Raman scattering. *Nature* **2013**, *498*, 82–86.

- (10) Jiang, S.; Zhang, Y.; Zhang, R.; Hu, C.; Liao, M.; Luo, Y.; Yang, J.; Dong, Z.; Hou, J. Distinguishing adjacent molecules on a surface using plasmon-enhanced Raman scattering. *Nat. Nanotechnol.* **2015**, *10*, 865–869.
- (11) Chiang, N.; Chen, X.; Goubert, G.; Chulhai, D. V.; Chen, X.; Pozzi, E. A.; Jiang, N.; Hersam, M. C.; Seideman, T.; Jensen, L.; Van Duyne, R. P. Conformational contrast of surface-mediated molecular switches yields Ångstrom-scale spatial resolution in ultrahigh vacuum tip-enhanced Raman spectroscopy. *Nano Lett.* **2016**, *16*, 7774–7778.
- (12) Benz, F.; Schmidt, M. K.; Dreismann, A.; Chikkaraddy, R.; Zhang, Y.; Demetriadou, A.; Carnegie, C.; Ohadi, H.; De Nijs, B.; Esteban, R., et al. Single-molecule optomechanics in “picocavities”. *Science* **2016**, *354*, 726–729.
- (13) Yang, B.; Chen, G.; Ghafoor, A.; Zhang, Y.; Zhang, Y.; Zhang, Y.; Luo, Y.; Yang, J.; Sandoghdar, V.; Aizpurua, J., et al. Sub-nanometre resolution in single-molecule photoluminescence imaging. *Nat. Photonics* **2020**, *14*, 693–699.
- (14) Liu, P.; Chulhai, D. V.; Jensen, L. Single-Molecule Imaging Using Atomistic Near-Field Tip-Enhanced Raman Spectroscopy. *ACS Nano* **2017**, *11*, 5094–5102.
- (15) Yuan, Y.; Zhou, L.; Robatjazi, H.; Bao, J. L.; Zhou, J.; Bayles, A.; Yuan, L.; Lou, M.; Lou, M.; Khatiwada, S., et al. Earth-abundant photocatalyst for H₂ generation from NH₃ with light-emitting diode illumination. *Science* **2022**, *378*, 889–893.
- (16) Ezendam, S.; Herran, M.; Nan, L.; Gruber, C.; Kang, Y.; Gröbmeyer, F.; Lin, R.; Gargiulo, J.; Sousa-Castillo, A.; Cortés, E. Hybrid plasmonic nanomaterials for hydrogen generation and carbon dioxide reduction. *ACS Energy Lett.* **2022**, *7*, 778–815.
- (17) Baldi, A.; Askes, S. H. Pulsed Photothermal Heterogeneous Catalysis. *ACS Catal.* **2023**, *13*, 3419–3432.
- (18) Herran, M.; Sousa-Castillo, A.; Fan, C.; Lee, S.; Xie, W.; Döblinger, M.; Auguie, B.; Cortés, E. Tailoring plasmonic bimetallic nanocatalysts toward sunlight-driven H₂ production. *Adv. Funct. Mater.* **2022**, *32*, 2203418.

- (19) Yuan, L.; Zhou, J.; Zhang, M.; Wen, X.; Martirez, J. M. P.; Robotjazi, H.; Zhou, L.; Carter, E. A.; Nordlander, P.; Halas, N. J. Plasmonic Photocatalysis with Chemically and Spatially Specific Antenna–Dual Reactor Complexes. *ACS Nano* **2022**, *16*, 17365–17375.
- (20) Baumberg, J. J. Picocavities: a primer. *Nano Lett.* **2022**, *22*, 5859–5865.
- (21) Li, S.; Miao, P.; Zhang, Y.; Wu, J.; Zhang, B.; Du, Y.; Han, X.; Sun, J.; Xu, P. Recent advances in plasmonic nanostructures for enhanced photocatalysis and electrocatalysis. *Adv. Mater.* **2021**, *33*, 2000086.
- (22) Gargiulo, J.; Berté, R.; Li, Y.; Maier, S. A.; Cortés, E. From optical to chemical hot spots in plasmonics. *Acc. Chem. Res.* **2019**, *52*, 2525–2535.
- (23) Mukherjee, S.; Libisch, F.; Large, N.; Neumann, O.; Brown, L. V.; Cheng, J.; Lassiter, J. B.; Carter, E. A.; Nordlander, P.; Halas, N. J. Hot electrons do the impossible: plasmon-induced dissociation of H₂ on Au. *Nano Lett.* **2013**, *13*, 240–247.
- (24) Clavero, C. Plasmon-induced hot-electron generation at nanoparticle/metal-oxide interfaces for photovoltaic and photocatalytic devices. *Nat. Photonics* **2014**, *8*, 95–103.
- (25) Robotjazi, H.; Bao, J. L.; Zhang, M.; Zhou, L.; Christopher, P.; Carter, E. A.; Nordlander, P.; Halas, N. J. Plasmon-driven carbon–fluorine (C(sp³)-F) bond activation with mechanistic insights into hot-carrier-mediated pathways. *Nat. Catal.* **2020**, *3*, 564–573.
- (26) Zhan, C.; Moskovits, M.; Tian, Z.-Q. Recent progress and prospects in plasmon-mediated chemical reaction. *Matter* **2020**, *3*, 42–56.
- (27) Dong, Y.; Hu, C.; Xiong, H.; Long, R.; Xiong, Y. Plasmonic Catalysis: New Opportunity for Selective Chemical Bond Evolution. *ACS Catal.* **2023**, *13*, 6730–6743.
- (28) Cortés, E.; Grzeschik, R.; Maier, S. A.; Schlücker, S. Experimental characterization techniques for plasmon-assisted chemistry. *Nat. Rev. Chem.* **2022**, *6*, 259–274.

- (29) Sa, J.; Wach, A.; Szlachetko, J.; Maximenko, A.; Sobol, T.; Partyka-Jankowska, E.; Bacellar, C.; Cirelli, C.; Johnson, P.; Castillo, R. G.; Silveira, V. R.; Broqvist, P.; Kullgren, J.; Halas, N.; Nordlander, P. The Dynamics of Plasmon-Induced Hot Carrier Creation in Colloidal Gold. **2024**, preprint, <https://www.researchsquare.com/article/rs-3799527/v1>, accessed by date 14 June 2024.
- (30) Rossi, T. P.; Erhart, P.; Kuisma, M. Hot-carrier generation in plasmonic nanoparticles: The importance of atomic structure. *ACS nano* **2020**, *14*, 9963–9971.
- (31) Liu, J. G.; Zhang, H.; Link, S.; Nordlander, P. Relaxation of plasmon-induced hot carriers. *ACS Photonics* **2017**, *5*, 2584–2595.
- (32) Sánchez, C. G.; Berdakin, M. Plasmon-induced hot carriers: An atomistic perspective of the first tens of femtoseconds. *J. Phys. Chem. C* **2022**, *126*, 10015–10023.
- (33) Wu, X.; van der Heide, T.; Wen, S.; Frauenheim, T.; Tretiak, S.; Yam, C.; Zhang, Y. Molecular dynamics study of plasmon-mediated chemical transformations. *Chem. Sci.* **2023**, *14*, 4714–4723.
- (34) Myroshnychenko, V.; Rodríguez-Fernández, J.; Pastoriza-Santos, I.; Funston, A. M.; Novo, C.; Mulvaney, P.; Liz-Marzan, L. M.; García de Abajo, F. J. Modelling the optical response of gold nanoparticles. *Chem. Soc. Rev.* **2008**, *37*, 1792–1805.
- (35) Hohenester, U.; Trügler, A. MNPBEM—A Matlab toolbox for the simulation of plasmonic nanoparticles. *Comput. Phys. Commun.* **2012**, *183*, 370–381.
- (36) García de Abajo, F. J.; Howie, A. Retarded field calculation of electron energy loss in inhomogeneous dielectrics. *Phys. Rev. B* **2002**, *65*, 115418.
- (37) Hao, F.; Nordlander, P. Efficient dielectric function for FDTD simulation of the optical properties of silver and gold nanoparticles. *Chem. Phys. Lett.* **2007**, *446*, 115–118.
- (38) Sehmi, H.; Langbein, W.; Muljarov, E. Optimizing the Drude-Lorentz model for material permittivity: Method, program, and examples for gold, silver, and copper. *Phys. Rev. B* **2017**, *95*, 115444.
- (39) Teperik, T. V.; Nordlander, P.; Aizpurua, J.; Borisov, A. G. Quantum effects and nonlocality in strongly coupled plasmonic nanowire dimers. *Opt. Express* **2013**, *21*, 27306–27325.

- (40) Zhu, W.; Esteban, R.; Borisov, A. G.; Baumberg, J. J.; Nordlander, P.; Lezec, H. J.; Aizpurua, J.; Crozier, K. B. Quantum mechanical effects in plasmonic structures with subnanometre gaps. *Nat. Commun.* **2016**, *7*, 11495.
- (41) Urbieto, M.; Barbry, M.; Zhang, Y.; Koval, P.; Sánchez-Portal, D.; Zabala, N.; Aizpurua, J. Atomic-Scale Lightning Rod Effect in Plasmonic Picocavities: A Classical View to a Quantum Effect. *ACS Nano* **2018**, *12*, 585–595.
- (42) Savage, K. J.; Hawkeye, M. M.; Esteban, R.; Borisov, A. G.; Aizpurua, J.; Baumberg, J. J. Revealing the quantum regime in tunnelling plasmonics. *Nature* **2012**, *491*, 574–577.
- (43) Marinica, D.; Kazansky, A.; Nordlander, P.; Aizpurua, J.; Borisov, A. G. Quantum plasmonics: nonlinear effects in the field enhancement of a plasmonic nanoparticle dimer. *Nano Lett.* **2012**, *12*, 1333–1339.
- (44) Esteban, R.; Borisov, A. G.; Nordlander, P.; Aizpurua, J. Bridging quantum and classical plasmonics with a quantum-corrected model. *Nat. Commun.* **2012**, *3*, 825.
- (45) Esteban, R.; Zugarramurdi, A.; Zhang, P.; Nordlander, P.; García-Vidal, F. J.; Borisov, A. G.; Aizpurua, J. A classical treatment of optical tunneling in plasmonic gaps: extending the quantum corrected model to practical situations. *Faraday Discuss.* **2015**, *178*, 151–183.
- (46) Campos, A.; Troc, N.; Cottancin, E.; Pellarin, M.; Weissker, H.-C.; Lermé, J.; Kociak, M.; Hillenkamp, M. Plasmonic quantum size effects in silver nanoparticles are dominated by interfaces and local environments. *Nat. Phys.* **2019**, *15*, 275–280.
- (47) Scholl, J. A.; García-Etxarri, A.; Koh, A. L.; Dionne, J. A. Observation of quantum tunneling between two plasmonic nanoparticles. *Nano Lett.* **2013**, *13*, 564–569.
- (48) Barbry, M.; Koval, P.; Marchesin, F.; Esteban, R.; Borisov, A.; Aizpurua, J.; Sánchez-Portal, D. Atomistic near-field nanoplasmonics: reaching atomic-scale resolution in nanooptics. *Nano Lett.* **2015**, *15*, 3410–3419.
- (49) Domenis, N.; Grobas Illobre, P.; Marsili, M.; Stener, M.; Toffoli, D.; Coccia, E. Time Evolution of Plasmonic Features in Pentagonal Ag Clusters. *Molecules* **2023**, *28*, 5671.

- (50) Herring, C. J.; Montemore, M. M. Recent Advances in Real-Time Time-Dependent Density Functional Theory Simulations of Plasmonic Nanostructures and Plasmonic Photocatalysis. *ACS Nanosci. Au* **2023**, *3*, 269–279.
- (51) Kuisma, M.; Sakko, A.; Rossi, T. P.; Larsen, A. H.; Enkovaara, J.; Lehtovaara, L.; Rantala, T. T. Localized surface plasmon resonance in silver nanoparticles: Atomistic first-principles time-dependent density-functional theory calculations. *Phys. Rev. B* **2015**, *91*, 115431.
- (52) Ding, F.; Guidez, E. B.; Aikens, C. M.; Li, X. Quantum coherent plasmon in silver nanowires: A real-time TDDFT study. *J. Chem. Phys.* **2014**, *140*, 244705.
- (53) Senanayake, R. D.; Lingerfelt, D. B.; Kuda-Singappulige, G. U.; Li, X.; Aikens, C. M. Real-time TDDFT investigation of optical absorption in gold nanowires. *J. Phys. Chem. C* **2019**, *123*, 14734–14745.
- (54) Baseggio, O.; Fronzoni, G.; Stener, M. A new time dependent density functional algorithm for large systems and plasmons in metal clusters. *J. Chem. Phys.* **2015**, *143*, 024106.
- (55) Baseggio, O.; De Vetta, M.; Fronzoni, G.; Stener, M.; Sementa, L.; Fortunelli, A.; Calzolari, A. Photoabsorption of icosahedral noble metal clusters: An efficient TDDFT approach to large-scale systems. *J. Phys. Chem. C* **2016**, *120*, 12773–12782.
- (56) Sinha-Roy, R.; Garcia-Gonzalez, P.; Weissker, H.-C.; Rabilloud, F.; Fernandez-Dominguez, A. I. Classical and ab Initio Plasmonics Meet at Sub-nanometric Noble Metal Rods. *ACS Photonics* **2017**, *4*, 1484–1493.
- (57) Giovannini, T.; Rosa, M.; Corni, S.; Cappelli, C. A classical picture of subnanometer junctions: an atomistic Drude approach to nanoplasmonics. *Nanoscale* **2019**, *11*, 6004–6015.
- (58) Bonatti, L.; Gil, G.; Giovannini, T.; Corni, S.; Cappelli, C. Plasmonic Resonances of Metal Nanoparticles: Atomistic vs. Continuum Approaches. *Front. Chem.* **2020**, *8*, 340.
- (59) Giovannini, T.; Bonatti, L.; Polini, M.; Cappelli, C. Graphene plasmonics: Fully atomistic approach for realistic structures. *J. Phys. Chem. Lett.* **2020**, *11*, 7595–7602.

- (60) Bonatti, L.; Nicoli, L.; Giovannini, T.; Cappelli, C. In silico design of graphene plasmonic hot-spots. *Nanoscale Adv.* **2022**, *4*, 2294–2302.
- (61) Zanutto, S.; Bonatti, L.; Pantano, M. F.; Miseikis, V.; Speranza, G.; Giovannini, T.; Coletti, C.; Cappelli, C.; Tredicucci, A.; Toncelli, A. Strain-induced plasmon confinement in polycrystalline graphene. *ACS Photonics* **2023**, *10*, 394–400.
- (62) Yamada, A. Classical electronic and molecular dynamics simulation for optical response of metal system. *J. Chem. Phys.* **2021**, *155*, 174118.
- (63) Huang, X.; Zhang, W.; Liang, W. Time-dependent Kohn- Sham electron dynamics coupled with nonequilibrium plasmonic response via atomistic electromagnetic model. *J. Chem. Phys.* **2024**, *160*, 214106.
- (64) Giovannini, T.; Bonatti, L.; Lafiosca, P.; Nicoli, L.; Castagnola, M.; Illobre, P. G.; Corni, S.; Cappelli, C. Do we really need quantum mechanics to describe plasmonic properties of metal nanostructures? *ACS photonics* **2022**, *9*, 3025–3034.
- (65) Nicoli, L.; Lafiosca, P.; Grobas Illobre, P.; Bonatti, L.; Giovannini, T.; Cappelli, C. Fully atomistic modeling of plasmonic bimetallic nanoparticles: nanoalloys and core-shell systems. *Front. Photonics* **2023**, *4*, 1199598.
- (66) Bade, W. Drude-Model Calculation of Dispersion Forces. I. General Theory. *J. Chem. Phys.* **1957**, *27*, 1280–1284.
- (67) Lafiosca, P.; Giovannini, T.; Benzi, M.; Cappelli, C. Going Beyond the Limits of Classical Atomistic Modeling of Plasmonic Nanostructures. *J. Phys. Chem. C* **2021**, *125*, 23848–23863.
- (68) Mayer, A. Formulation in terms of normalized propagators of a charge-dipole model enabling the calculation of the polarization properties of fullerenes and carbon nanotubes. *Phys. Rev. B* **2007**, *75*, 045407.
- (69) Pinchuk, A.; Kreibig, U.; Hilger, A. Optical properties of metallic nanoparticles: influence of interface effects and interband transitions. *Surf. Sci.* **2004**, *557*, 269–280.

- (70) Pinchuk, A.; Von Plessen, G.; Kreibig, U. Influence of interband electronic transitions on the optical absorption in metallic nanoparticles. *J. Phys. D: Appl. Phys.* **2004**, *37*, 3133.
- (71) Balamurugan, B.; Maruyama, T. Evidence of an enhanced interband absorption in Au nanoparticles: size-dependent electronic structure and optical properties. *Appl. Phys. Lett.* **2005**, *87*, 143105.
- (72) Liebsch, A. Surface-plasmon dispersion and size dependence of Mie resonance: silver versus simple metals. *Phys. Rev. B* **1993**, *48*, 11317.
- (73) Santiago, E. Y.; Besteiro, L. V.; Kong, X.-T.; Correa-Duarte, M. A.; Wang, Z.; Govorov, A. O. Efficiency of hot-electron generation in plasmonic nanocrystals with complex shapes: surface-induced scattering, hot spots, and interband transitions. *ACS Photonics* **2020**, *7*, 2807–2824.
- (74) Giovannini, T.; Puglisi, A.; Ambrosetti, M.; Cappelli, C. Polarizable QM/MM approach with fluctuating charges and fluctuating dipoles: the QM/FQF μ model. *J. Chem. Theory Comput.* **2019**, *15*, 2233–2245.
- (75) Dall’Osto, G.; Gil, G.; Pipolo, S.; Corni, S. Real-time dynamics of plasmonic resonances in nanoparticles described by a boundary element method with generic dielectric function. *J. Chem. Phys.* **2020**, *153*, 184114.
- (76) Vanden-Eijnden, E.; Ciccotti, G. Second-order integrators for Langevin equations with holonomic constraints. *Chem. Phys. Lett.* **2006**, *429*, 310–316.
- (77) Wales, D. J.; Doye, J. P. Global optimization by basin-hopping and the lowest energy structures of Lennard-Jones clusters containing up to 110 atoms. *J. Phys. Chem. A* **1997**, *101*, 5111–5116.
- (78) Newville, M.; Stensitzki, T.; Allen, D. B.; Ingargiola, A. LMFIT: Non-Linear Least-Square Minimization and Curve-Fitting for Python. **2015**, <https://doi.org/10.5281/zenodo.11813>.
- (79) Virtanen, P. et al. SciPy 1.0: Fundamental Algorithms for Scientific Computing in Python. *Nat. Methods* **2020**, *17*, 261–272.
- (80) Marchesin, F.; Koval, P.; Barbry, M.; Aizpurua, J.; Sánchez-Portal, D. Plasmonic response of metallic nanojunctions driven by single atom motion: quantum transport revealed in optics. *ACS Photonics* **2016**, *3*, 269–277.

- (81) Liu, L.; Wang, Y.; Fang, Z.; Zhao, K. Plasmon hybridization model generalized to conductively bridged nanoparticle dimers. *J. Chem. Phys.* **2013**, *139*, 064310.
- (82) Pérez-González, O.; Zabala, N.; Aizpurua, J. Optical characterization of charge transfer and bonding dimer plasmons in linked interparticle gaps. *New J. Phys.* **2011**, *13*, 083013.
- (83) Duan, H.; Fernández-Domínguez, A. I.; Bosman, M.; Maier, S. A.; Yang, J. K. Nanoplasmonics: classical down to the nanometer scale. *Nano Lett.* **2012**, *12*, 1683–1689.
- (84) Rossi, T. P.; Zugarramurdi, A.; Puska, M. J.; Nieminen, R. M. Quantized evolution of the plasmonic response in a stretched nanorod. *Phys. Rev. Lett.* **2015**, *115*, 236804.
- (85) Varas, A.; García-González, P.; Feist, J.; García-Vidal, F.; Rubio, A. Quantum plasmonics: from jellium models to ab initio calculations. *Nanophotonics* **2016**, *5*, 409–426.
- (86) Zhang, P.; Feist, J.; Rubio, A.; García-González, P.; García-Vidal, F. Ab initio nanoplasmonics: The impact of atomic structure. *Phys. Rev. B* **2014**, *90*, 161407.
- (87) Khurgin, J. B.; Levy, U. Generating hot carriers in plasmonic nanoparticles: when quantization does matter? *ACS Photonics* **2020**, *7*, 547–553.
- (88) Khurgin, J.; Tsai, W.-Y.; Tsai, D. P.; Sun, G. Landau damping and limit to field confinement and enhancement in plasmonic dimers. *ACS Photonics* **2017**, *4*, 2871–2880.
- (89) Lafiosca, P.; Nicoli, L.; Bonatti, L.; Giovannini, T.; Corni, S.; Cappelli, C. Qm/classical modeling of surface enhanced Raman scattering based on atomistic electromagnetic models. *J. Chem. Theory Comput.* **2023**, *19*, 3616–3633.
- (90) Illobre, P. G.; Lafiosca, P.; Guidone, T.; Mazza, F.; Giovannini, T.; Cappelli, C. Multiscale Modeling of Surface Enhanced Fluorescence. *Nanoscale Adv.* **2024**, <http://dx.doi.org/10.1039/D4NA00080C>.
- (91) Pipolo, S.; Corni, S. Real-time description of the electronic dynamics for a molecule close to a plasmonic nanoparticle. *J. Phys. Chem. C* **2016**, *120*, 28774–28781.

- (92) Marsili, M.; Corni, S. Electronic dynamics of a molecular system coupled to a plasmonic nanoparticle combining the polarizable continuum model and many-body perturbation theory. *J. Phys. Chem. C* **2022**, *126*, 8768–8776.
- (93) Coccia, E.; Fregoni, J.; Guido, C.; Marsili, M.; Pipolo, S.; Corni, S. Hybrid theoretical models for molecular nanoplasmonics. *J. Chem. Phys.* **2020**, *153*, 200901.
- (94) Dall’Osto, G.; Marsili, M.; Vanzan, M.; Toffoli, D.; Stener, M.; Corni, S.; Coccia, E. Peeking into the Femtosecond Hot-Carrier Dynamics Reveals Unexpected Mechanisms in Plasmonic Photocatalysis. *J. Am. Chem. Soc.* **2024**, *146*, 2208–2218.